RSC Advances

ROYAL SOCIETY OF CHEMISTRY

www.rsc.org/advances

Following heterogeneous nucleation of CO_2 on H_2O ice nanoparticles with microsecond resolution

Shinobu Tanimura, [a] Yensil Park,[a] Andrew Amaya,[a] Viraj Modak,[a] and Barbara E. Wyslouzil[ab]

[a] *William G. Lowrie Department of Chemical and Biomolecular Engineering, The Ohio State University, 151 West Woodruff Av., Columbus, Ohio 43210, USA*

[b] *Department of Chemistry, The Ohio State University, 100 West 18th Avenue, Columbus, Ohio 43210, USA*

Abstract

Heterogeneous nucleation of CO_2 onto H_2O ice particles may play an important role in proposed innovative CO_2 capture technologies, as well as in the formation of Martian clouds. In this work we follow the nucleation/condensation of CO_2/H_2O gas mixtures with microsecond resolution in supersonic Laval nozzles using pressure trace measurement (PTM) and small angle x-ray scattering (SAXS). The latent heat release detected by the PTM reveals that the first phase transition in the expanding CO_2/H_2O mixture is the formation of H_2O ice particles by the homogeneous nucleation/condensation and freezing of H_2O. This is followed by the heterogeneous nucleation and growth of CO_2 on the H_2O ice particles. The onset conditions for heterogeneous nucleation, i.e. the partial pressure of CO_2 and temperature from PTM and the radius of gyration of the H_2O ice particles from SAXS, were determined in the temperature range 124 to 146 K and for particles with radii of gyration in range of 2.1 to 4.3 nm. The onset conditions suggest that the heterogeneous nucleation of CO_2 may start from the supercooled liquid phase under our conditions. Downstream of the onset point, the partial pressure of CO_2 and temperature rapidly approach the vapor-solid equilibrium line of CO_2, demonstrating that even if CO_2

condensation is initiated by heterogeneous nucleation of the liquid phase, it proceeds via growth of the solid.

1. Introduction

Heterogeneous nucleation of carbon dioxide (CO_2) onto pre-existing, frozen H_2O particles may play an important role in innovative technological processes. In a proposed low-temperature CO_2 capture technology, for example, flue gas cools as it expands in a supersonic nozzle driving CO_2 deposition, and the CO_2 particles generated are subsequently separated from the gas by centrifugal forces.[1,2] Under the conditions where the CO_2 capture technology is to be applied, however, H_2O vapor is also present.[2,3] As illustrated in **Fig. 1**, the low vapor pressure of H_2O relative to CO_2 suggests that even with reasonable levels of H_2O vapor removal from the gas stream, pure H_2O will still condense in the supersonic nozzle at much higher temperatures than pure CO_2 does. Based on this phase diagram, we expect that condensation from a CO_2/H_2O mixture expanding in a supersonic flow is initiated by the homogeneous nucleation of H_2O. The H_2O droplets grow and solidify as the temperature drops during the continued expansion, and finally CO_2 condenses/deposits heterogeneously on the H_2O ice particles. Although this intuitive picture is appealing, there are no experimental results that confirm the prediction, or report the degree of CO_2 saturation required to drive heterogeneous nucleation under the rapid cooling conditions characteristic of supersonic flows.

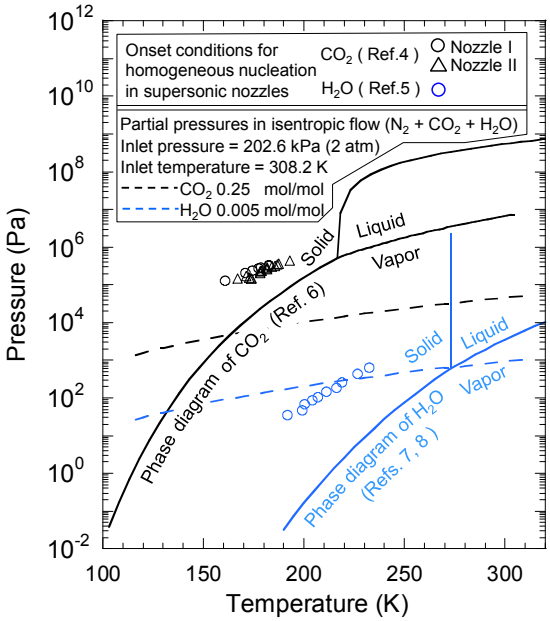

Fig.1 Phase diagram and onset conditions for unary homogeneous nucleation of CO_2 or H_2O. Partial pressures of condensable species in isentropic flow (non-condensing flow) under a set of conditions in this study are also shown. These conditions are, for example, close to the typical conditions of the flue gas of an iron production process (Corex process),[9] temperature 313 K, pressure 3.5 atm, CO_2 0.24 - 0.30 mol/mol, and H_2O 0.01 mol/mol.

Earlier studies of heterogeneous nucleation of CO_2 on H_2O ice have largely been motivated by the fact that this process is a possible pathway for the formation of CO_2 clouds in the Martian atmosphere.[10,11] Glandorf et al. monitored the deposition of CO_2 on

flat H_2O ice films under conditions that mimicked the Martian atmosphere (T = 130.2 - 140.0 K) using transmission Fourier transform infrared (FTIR) spectroscopy.[10] They reported that heterogeneous nucleation, at a rate of ~ 1 $cm^{-2}s^{-1}$, required a saturation with respect to CO_2 solid of ~1.34 and that the contact parameter between solid CO_2 and solid H_2O was 0.95. A contact parameter less than unity, i.e. a contact angle larger than zero, is consistent with the results of the temperature programmed desorption (TPD) measurements for CO_2 on H_2O ice surfaces of Noble et al.,[12] that suggested CO_2 deposited on H_2O ice preferentially forms clusters (or islands). Other FTIR studies involving CO_2/H_2O aerosols[11,13,14] focused on the structure and structural evolution of the particles rather than characterizing the conditions required to initiate heterogeneous nucleation. They also reported that heterogeneous nucleation of CO_2 onto H_2O ice particles yielded an architecture consisting of CO_2 patches on the underlying ice rather than a perfectly coated core-shell structure. These experimental results stand in contrast to recent classical molecular dynamics simulations of the deposition of CO_2 onto H_2O ice that showed the CO_2 molecules fully wet the H_2O ice surface.[15]

To the best of our knowledge there are no experiments that have directly followed the heterogeneous nucleation of CO_2 onto H_2O ice particles. Here we report our efforts to study this phenomenon by conducting experiments in our supersonic nozzle apparatus. Under steady flow conditions we can follow the progression of nucleation/condensation with a time resolution better than several μs, by changing the measurement position from upstream to downstream in the nozzle. Static pressure trace measurements (PTM) of the supersonic flow of CO_2/H_2O mixtures in nitrogen (N_2) gas provide the gas temperature, and the heat release due to CO_2/H_2O phase changes. We find which species is involved in the detected phase change by investigating the dependence of the heat release on the composition of the CO_2/H_2O gas mixture, and we determine the onset conditions (partial pressure of the condensable species and temperature) for that phase change. From the size of the condensed particles determined by small angle x-ray scattering (SAXS) measurements, we examine how the onset conditions for heterogeneous nucleation depend

on the size of the seed particle. The structure of the resultant particles is the subject of ongoing research and is not discussed here.

2. Experimental

2.1. Flow system and nozzles

Two modifications were made to our previous experimental setup[16] in order to supply the condensable species, CO_2 and H_2O, as shown in **Fig. 2**. The first change is the addition of a CO_2 cylinder that is connected to the main flow through a mass flow controller (Type 1559A, 151.1 standard liter/min (SLM); MKS). Although the pressurized CO_2 liquid in the cylinder (~60 atm) is at room temperature, the temperature of the CO_2 gas drops significantly as it expands adiabatically across the regulator. An inline heater was therefore added to the exit of the CO_2 gas cylinder to prevent the deposition of solid CO_2 in the regulator.

The second modification is that we pressurized the H_2O (liquid) bottle by connecting it to the flow tube just upstream of the vapor generator. In the current experiments the pressure at the system near the water injection point is around 2.8 atm and this change ensures that the pressures at the inlet and outlet of the peristaltic pump are almost the same, thereby stabilizing the H_2O flow rate.

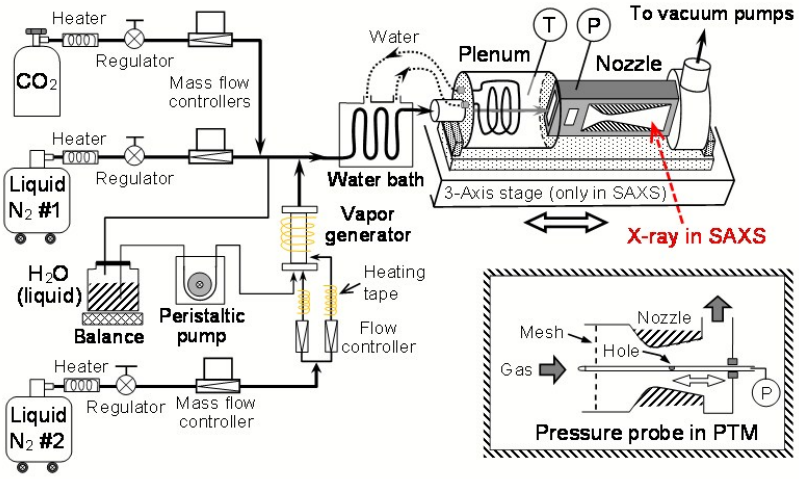

Fig.2 Experimental set up with a supersonic Laval nozzle. The inset at lower right illustrates the set up for pressure trace measurement

When the system is running, two high-pressure liquid N_2 Dewars (#1 and #2) connected to inline electrical heaters provide up to 20 mol/min of room temperature carrier gas. The flow rate of N_2 from the Dewars is controlled by mass flow controllers (Type 1559A, 200 and 400 SLM; MKS), each calibrated to an accuracy of 1 % of reading. Gas from Dewar #2 is heated to about 40-50 ˚C before entering the vapor generator. Here, the condensable liquid (H_2O) is fed into the system using a peristaltic pump, and part of the N_2 disperses that liquid into a fine spray. The remaining N_2 provides the energy to evaporate the droplets and further dilute the condensable vapor. The flow from the vapor generator merges with the main N_2/CO_2 flow supplied by Dewar #1 and the CO_2 cylinder. The mixed gas flows through a heat exchanger and enters the plenum where the final temperature adjustment is made. The stagnation temperature T_0 is measured in the plenum, using a high accuracy platinum resistance thermometer (RTD). The stagnation pressure p_0 is determined by measuring the static pressure in the region of the nozzle with constant cross sectional area, and correcting for the velocity of the gas. After leaving the plenum, the gas flows through the nozzle and is discharged to the atmosphere through 75 mm tubing by two rotary vane vacuum pumps (Type R5 RA0305D, 0.1 m^3/s displacement for each pump; Busch).

For all of the experiments conducted here the desired stagnation temperature T_0 was 15.0 ˚C (288.2 ± 0.05 K) or 35.0 ˚C (308.2 ± 0.05 K), and the stagnation pressure p_0 was set to 2.00 atm (202.6 ± 0.4 kPa). When the flow rate of N_2 exceeds the total capacity of the two mass flow controllers, 200 + 400 = 600 SLM, the third liquid N_2 Dewar was connected to the main flow via a mass flow controller (Type 1559A, 215.8 SLM; MKS) in a manner similar to Dewar #1. The H_2O liquid used in this study was deionized water with a resistivity greater than 10 MΩ·cm or distilled water with a resistivity of 1 MΩ·cm. Preliminary experiments confirmed that CO_2 gases with purities of 99.9 % and 99.99 % gave the same experimental results. Thus, the lower purity CO_2 (99.9 %) was used in most experiments in this study.

We used conventional Laval nozzles with rectangular cross sections. Two nozzles, Nozzle T1 and T3, characterized by different nominal expansion rates and flat-plate side

walls were used for the PTM. Two additional nozzles, Nozzle T1_mica and Nozzle T3_mica, with the same nominal expansion rates as Nozzle T1 and Nozzle T3, respectively, but with mica windows in the sidewalls, were used for SAXS experiments. Further details regarding the dimensions of the nozzles are given in Appendix 1.

2.2. Pressure trace measurement

In the pressure trace measurement (PTM), we measure the static pressure along the length of the nozzle using a movable static pressure probe (see the inset at lower right in Fig. 2). The probe is a 0.92 mm outside diameter stainless steel tube sealed at the upstream tip and with 2 equally spaced holes drilled ~310 mm downstream from the tip.

We also measured the static pressure at the physical throat, where the cross section of the nozzle reaches a minimum, through a small hole (0.34 mm diameter) in the shaped nozzle block in Fig. 14(b). By comparing the pressure at the physical throat with the pressure profile measured by the pressure probe, the distance between the physical throat and the effective throat can be determined. The latter is defined as the position where the effective flow area reaches a minimum and, the pressure ratio (≡ pressure at the effective throat/stagnation pressure) takes on the value, $p^*/p_0 = \{2/(\gamma+1)\}^{\gamma/(\gamma-1)}$ for constant specific heat ratio, γ.[17] When the heat capacity is strongly temperature dependent, as is the case for CO_2, the correct value of p^*/p_0 is determined by using the integration scheme detailed in the Appendix of Ref. 18. The distance between the physical throat and the effective throat is required in order to combine the data measured by PTM and SAXS, because the pressure profile is measured as a function of the distance from the effective throat, while the spectra are measured as a function of the distance from the physical throat. For the remainder of this paper the term "throat" will mean the effective throat unless otherwise indicated. The stagnation conditions for the PTMs are summarized in Table 1 together with those for the SAXS measurements.

2.3. Small angle x-ray scattering measurement

The SAXS measurements were performed using the 12-ID_C beamline at the Advanced Photon Source (APS), Argonne National Laboratories, Argonne, IL. In the SAXS measurements, we used a 0.2 x 0.2 mm^2 beam of 12 keV (λ = 0.10 nm) x-rays with a wavelength spread $\Delta\lambda/\lambda = 10^{-4}$. The x-rays were detected by a two-dimensional detector with a 17 x 17 cm^2 active area, which consists of four 1024 x 1024 pixel charge coupled device chips. The sample-to-detector distance was 2.262 m. One-dimensional scattering spectra were obtained by averaging the two-dimensional data using the APS data inversion program. To make the SAXS measurements as a function of position in the nozzle, we mounted the plenum, supersonic nozzle, and a section of vacuum tubing on a 3-axis motorized stage as shown in Fig. 2.

3. Analytical methods

3.1. Analysis of PTM results

The temperature, mass density, and velocity of the flowing gas mixture, and the heat released due to the phase changes and mass fractions of condensates (CO_2 and H_2O) were derived from the static pressure profile determined by PTM by integrating the one-dimensional adiabatic steady flow equations.[19] In order to solve the flow equations for the binary condensation, we made the same assumption as in Ref. 19, i.e.,

$$\frac{p_{v\_i}}{p_{v\_j}} = \frac{p_i^{mix}\left(T, x_i^{\mathrm{av}}, x_j^{\mathrm{av}}\right)}{p_j^{mix}\left(T, x_i^{\mathrm{av}}, x_j^{\mathrm{av}}\right)}, \qquad (1)$$

where p_{v_i} (p_{v_j}) is the partial pressure of species i (j) in the vapor phase, and $x^{\mathrm{av}}{}_i$ ($x^{\mathrm{av}}{}_j$) is the average mole fraction of species i (j) in the condensate. The variable in the right side, $p^{\mathrm{mix}}{}_i$ ($p^{\mathrm{mix}}{}_j$) denotes the equilibrium vapor pressure of species i (j) over the bulk liquid at temperature T and mole fractions $x^{\mathrm{av}}{}_i$ and $x^{\mathrm{av}}{}_j$. The value of $p^{\mathrm{mix}}{}_i$ is calculated as $p^{\mathrm{mix}}{}_i = p_i x^{\mathrm{av}}{}_i \gamma_i$, where p_i is the equilibrium vapor pressure of the pure condensed species i and γ_i is the activity coefficient of species i in the condensed phase.

For CO_2 and H_2O mixtures, $p_{CO2} >> p_{H2O}$, and analysis of the PTM based on eqn (1) should match the process described in the Introduction (Figure 1). That is, initially only H_2O condenses until the H_2O in the vapor phase is completely exhausted, and CO_2 only starts to condense after that. Here, we ignore the small amount of CO_2 that will adsorb to the surface of the particles prior to nucleation/condensation since the heat released by this process is too small to detect.

The assumption expressed by eqn (1) determines the compositions (ratio between the concentrations of CO_2 and H_2O) in the vapor and condensed phases, and hence, can affect the thermodynamic properties of the gas mixture. Under our conditions, however, this effect is insignificant, because the concentration of H_2O is so low ($w_{CO2} \leq 0.346$ and $w_{H2O} \leq 0.0031$ as shown in Table 1) that the properties of the gas mixture are dominated by those of N_2 and CO_2.

Any effect of eqn (1) on the heat release determined for the phase change should be neglegible, and we can investigate the process of the nucleation/condensation of CO_2/H_2O mixture in the supersonic flow based on the heat release derived from the PTM with eqn (1) even if this assumption is not entirely correct. The analytical result is insensitive to the accuracy of the determinations of $p^{mix}{}_i$ and $p^{mix}{}_j$ in eqn (1), because $p_{CO2} >> p_{H2O}$, therefore, γ_i and γ_j were assumed to be unity for simplicity.

In our earlier work we have shown that the displacement thickness of the boundary layer on the nozzle surface is affected by condensation, and $(A/A^*)_{wet}$ deviates from $(A/A^*)_{dry}$ downstream of the onset point of condensation, where $(A/A^*)_{wet}$ and $(A/A^*)_{dry}$ denote the effective flow area ratios in condensing flow and non-condensing flow, respectively.[20] In order to determine $(A/A^*)_{wet}$, an additional parameter must be measured beyond the static pressure. In this study, we first analyze the PTM results assuming $(A/A^*) = (A/A^*)_{dry}$, and, if necessary, use the results of SAXS or a reasonable alternative assumption to determine the $(A/A^*)_{wet}$ in order to improve the accuracy of the analysis.

The thermodynamic properties of the materials used in this work are summarized in Appendix 2.

3.2. Analysis of the SAXS measurements

In the current experiments we found that the SAXS spectra of the H_2O or H_2O/CO_2 aerosol could not, in most cases, be modelled as scattering from a collection of polydisperse spheres. For the H_2O particles, we expect that this arises because the low temperatures and rapid cooling rates characteristic of the current experiments prevent full scintering as particles coagulate. Futhermore, the H_2O/CO_2 particles may adopt a non-spherical shape as suggested by mid-infrared extinction spectroscopies.[11,13,14] The question of particle structure is the subject of ongoing research, and in this study we characterize particle size by using the model independent Guinier analysis[21] to determine the radius of gyration of the particles.

According to the Guinier law, scattering intensity $I(q_s)$ is expressed by eqn (2) in the limit of small q_s as,

$$I(q_s) = I(0)exp\left(-\frac{1}{3}q_s^2 r_G^2\right), \qquad (2)$$

where q_s is the scattering vector (momentum transfer vector), and r_G denotes the radius of gyration. The radius of gyration can, therefore, be determined from the slope of the Guinier plot, $\ln[I(q_s)]$ vs q_s^2.

4. Experimental results and discussion

4.1. Phase changes detected by pressure trace measurements

Fig. 3(a) illustrates a typical pressure profile measured in Nozzle T1 together with the derived temperature profile. The isentropic pressure p_{is} and temperature T_{is} profiles are also shown, where these values correspond to the fictitious expansion of a gas mixture with the same physical properties as those of the condensing gas mixture but where neither condensation nor clustering occur. It is clear in Fig. 3(a) that T deviates from T_{is} in two distinct steps, suggesting two distinct phase transitions, where the first deviation is observed around z = 1 cm, and the start of the second one is around z = 8 cm. Applying our

conventional criterion for the onset of condensation, T - T_{is} = 0.5 K, we find that the first deviation starts at z = 0.6 cm.

To identify the nature of these phase transitions we turn to **Fig. 3(b).** This figure shows the partial pressures of CO_2 and H_2O in the isentropic flow, as well as the pressures required for the onset of CO_2 and H_2O condensation initiated by homogeneous unary nucleation of each species in supersonic flow. The latter come from empirical equations for the onset pressure, p_{on} = $a_0\exp(a_1T)$, that we derived by fitting to the experimental results in Ref. 4 for p_{on_CO2} and in Ref. 5 for p_{on_H2O}. The two equations for p_{on_CO2} correspond to the measurements made in Duff's Nozzle I ($d(A/A^*)/dz$ = ~0.7 cm^{-1}) in the temperature range160.8 ≤ T/K ≤ 182.6, and Nozzle II ($d(A/A^*)/dz$ = ~0.07 cm^{-1}) at temperatures 167.2 ≤ T/K ≤ 193.1. The equation for p_{on_H2O} corresponds to measurements in Khan et al's nozzle ($d(A/A^*)/dz$ = 0.0477 cm^{-1}) at temperatures 191.7 ≤ T/K ≤ 232.4. The expansion rate of Nozzle T1 ($d(A/A^*)/dz$ = ~0.17 cm^{-1}) is intermediate to those of Duff's nozzles and a factor of ~ 3.6 times higher than Khan et al's nozzle. Although onset conditions depend on the expansion rate of the nozzle, this dependence is not strong and our equations should be accurate enough to determine whether homogeneous nucleation is possible and, if so, to estimate the onset points in Nozzle T1.

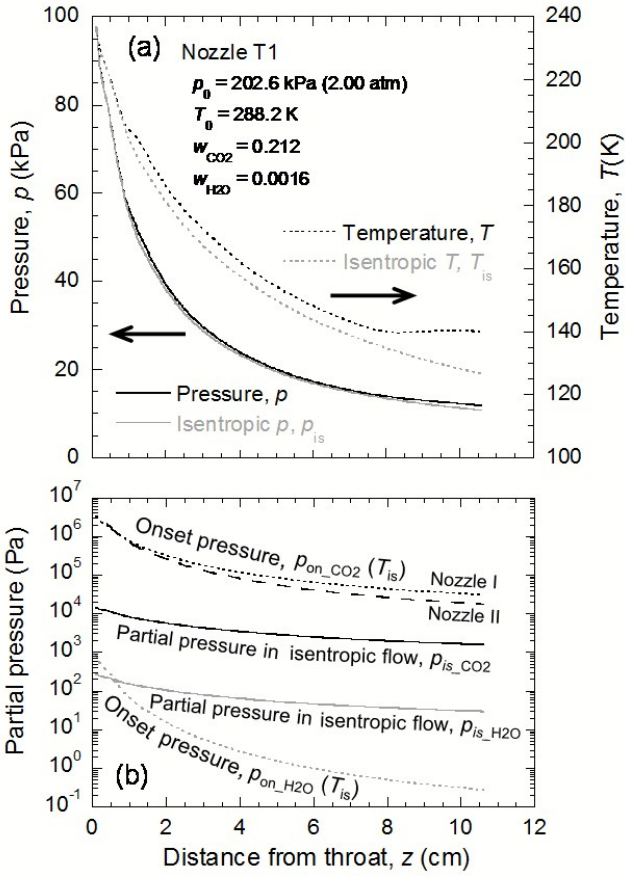

Fig.3 Typical results of PTM.
(a) Pressures and temperatures.
(b) Partial pressures of CO_2 and H_2O compared with the corresponding onset pressures required for homogeneous nucleation of the pure species, respectively.

As shown in Fig. 3(b), the onset pressure of CO_2 lies 1 - 2 orders of magnitude above the isentropic partial pressure of CO_2 in the experiment, thereby confirming that homogeneous nucleation of pure CO_2 cannot occur in Nozzle T1 under these conditions. In fact, similar analysis precludes homogeneous nucleation of pure CO_2 under any conditions used in this study. In contrast, for H_2O the p_{is_H2O} line crosses the p_{on_H2O} line at z = 0.6 cm, the location where we first observe T deviate from T_{is} in Fig. 3(a). This observation strongly suggests the first deviation of T from T_{is} is caused by condensation of H_2O initiated by homogeneous nucleation of H_2O.

In order to confirm this finding, we investigated the latent heat, q, release profiles derived from the PTMs for a series of experiments with a constant H_2O mass fraction and CO_2 mass fractions varying from 0 to 0.309. **Fig. 4** shows these profiles, labeled (1) – (5), for experiments conducted in Nozzle T1, where the thick black solid line corresponds to the experiment illustrated in Fig. 3. For z < 6 cm, all of the profiles align except for small fluctuations. In particular, q starts to increase at z = 0.6 - 0.8 cm and, after a steep increase, reaches a constant value near z = ~1.5 cm that persists as long as z < 6 cm. Hence, it is clear that CO_2 does not contribute to the phase change detected by the first increase in q, and that the initial heat release is solely due to the homogeneous nucleation/condensation of H_2O.

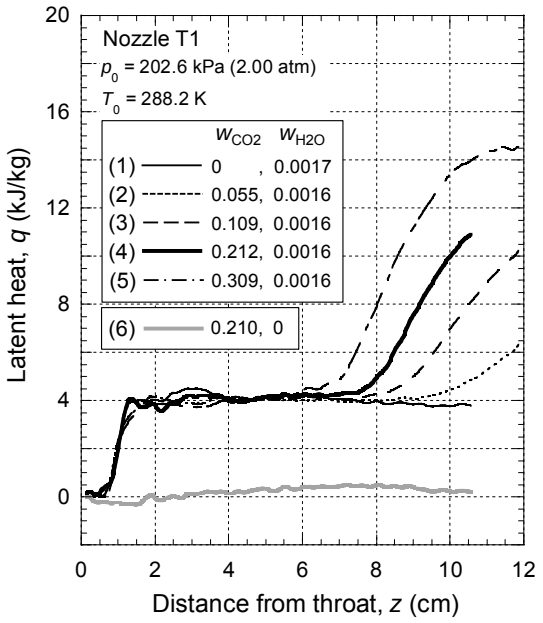

Fig.4 Latent heat released per unit mass of gas mixture, q

For experiments (1) – (5) in Fig. 4, the temperature at z = 6 cm is less than 150 K, a value that is far below the lowest temperature, 202 K, at which Manka et al.[22] observed the onset of H_2O droplet freezing in a supersonic nozzle. Hence, the H_2O droplets produced in Nozzle T1 should freeze well before reaching this point. Furthermore, since the vapor

pressure of H_2O ice is only 6 x 10^{-6} Pa at T = 150 K,[8] by this point in the expansion, almost all of the H_2O molecules in the core of the flow should be in the condensed phase.

Thus, the second heat release, observed when z > 6 cm in the flows (2) – (5) that contain both H_2O and CO_2, must be due to a CO_2 phase change. The fact that no heat is released in flow (6), where CO_2 is the only condensable species, confirms our earlier analysis that homogeneous nucleation of CO_2 cannot occur under the conditions in this study. We therefore attribute the second increase in q to the heterogeneous nucleation of CO_2 on the H_2O ice particles.

On the basis of PTM alone, we can confirm our intuitive picture that as the CO_2/H_2O mixture expands in the supersonic flow, H_2O ice particles are first produced by homogeneous nucleation and subsequent freezing. A further decrease in the temperature then drives the heterogeneous nucleation of CO_2 onto the H_2O ice particles.

4.2. Determining the onset conditions for heterogeneous nucleation of CO_2 on H_2O ice particle in Nozzle T1

In our earlier homogeneous nucleation studies in supersonic nozzles, the onset point was defined as the position where the gas temperature derived from PTM is 0.5 K higher than the isentropic temperature.[23] At the onset point for the heterogeneous nucleation of CO_2 on H_2O ice particles, however, the temperature has already deviated from the isentropic value due to the condensation of H_2O.

In this study we therefore determined the onset point for heterogeneous nucleation of CO_2 from the latent heat, q, release curves. As illustrated in **Fig. 5**, we first fit a straight line (broken line) to q between the first and second onset points and used this as the base line. A quadratic curve (dotted line) was then fit to the q values downstream of the second

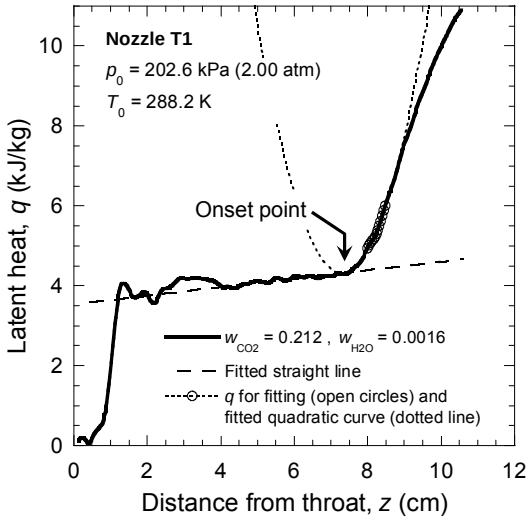

Fig.5 The method used to determine the onset point for heterogeneous nucleation of CO_2 on H_2O ice particle.

onset point using the constraint that this curve is tangent to the straight line. The tangent point between the quadratic curve and the straight base line was defined as the onset point. The quadratic curve fit was restricted to values of q that were 0.52 to 1.56 kJ/kg above the baseline, which corresponds to an increase in temperature of 0.5 - 1.5 K for pure nitrogen gas at 298.15 K.

A subtle point to consider here is that heat release to a supersonic flow can affect boundary layer development, and hence the values of the variables (T, q, g_{CO2}, g_{H2O}, u, ρ) estimated from the PTM downstream of the onset of condensation, where g_{CO2} and g_{H2O} denote mass fractions of condensates of CO_2 and H_2O, respectively, and u and ρ are the velocity and mass density of gas mixture, respectively. Fortunately, as discussed in Appendix 3, for the experiments conducted in nozzle T1 the effect of H_2O condensation on the boundary layer was negligible and we could assume $(A/A^*)_{wet} = (A/A^*)_{dry}$ prior to CO_2 condensation.

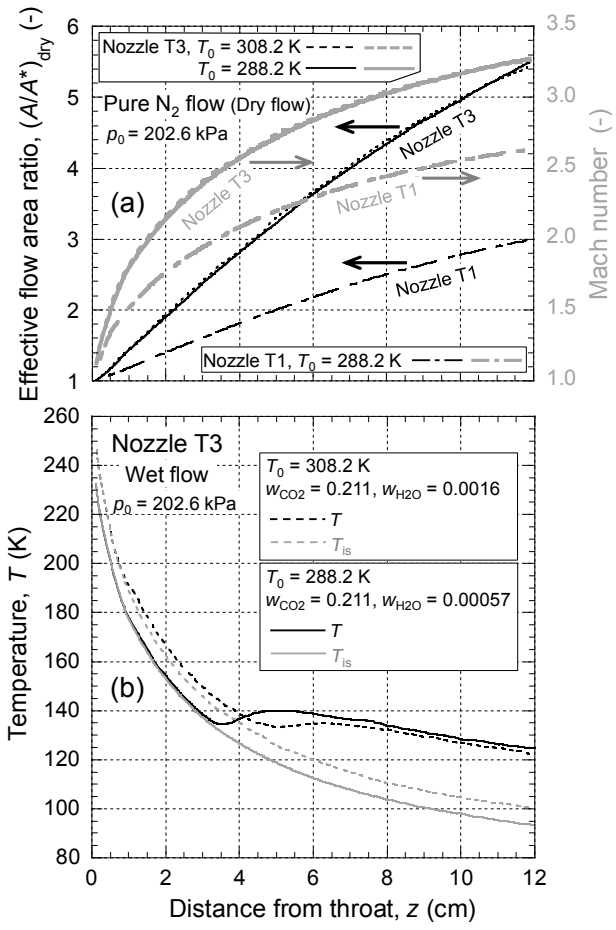

Fig.6 Flow properties in Nozzle T3.
(a) $(A/A^*)_{dry}$ and Mach number compared with those in Nozzle T1, respectively.
(b) Typical temperature profiles corresponding to experiments in Nozzle T3 at the same CO_2 partial pressure and different H_2O partial pressures.

4.3. Analytical results of pressure trace measurements with Nozzle T3 for determining the onset conditions for heterogeneous nucleation of CO_2 on H_2O ice particle

Although experiments in Nozzle T1 let us confirm the basic physics, nucleation of CO_2 on ice occurred fairly close to the end of the nozzle and we were not able to follow aerosol evolution to the

point where CO_2 condensation was complete. In order to do so we designed a faster nozzle, T3, and **Fig. 6(a)** illustrates the effective flow area ratios, $(A/A^*)_{dry}$, and Mach numbers for pure nitrogen flows at two inlet temperatures. The results in Nozzle T1 are also shown for comparison. The data in this figure confirm that such small changes in temperature do not affect A/A^* and Mach number, and that the expansion rate, $d(A/A^*)/dz$ = ~0.38 cm^{-1}, of Nozzle T3 is 2.2 times that of Nozzle T1, ~0.17 cm^{-1}.

Typical temperature profiles in Nozzle T3 are illustrated in **Fig. 6(b)**, and exhibit the same features as those observed in Nozzle T1. In particular, the first small deviation of T from T_{is} occurs at the onset point for the homogeneous nucleation of H_2O, and the deviation is almost constant until the second stronger deviation starts due to the heterogeneous nucleation of CO_2.

The onset conditions for hetergeneous nucleation of CO_2 on H_2O ice particle in Nozzle T3 were determined from the q profiles shown in **Fig. 7** using the method described above for Nozzle T1. In analyzing the nozzle T3 data, however, we found that we did need to correct for the deviation of $(A/A^*)_{wet}$ from $(A/A^*)_{dry}$ in the flows with higher water content illustrated in Figs. 7(b) and 7(c).The approach we used to do so is outlined in Appendix 3.

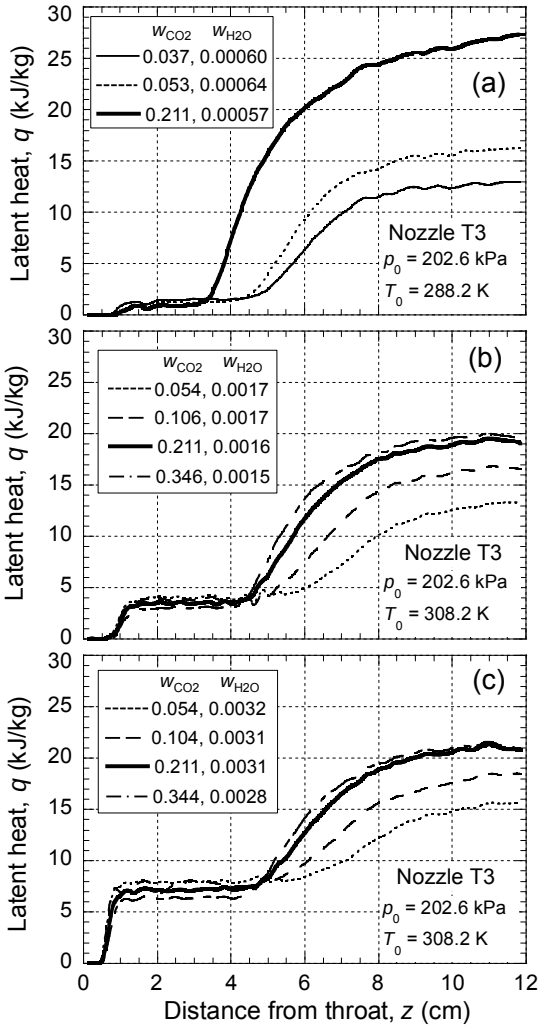

Fig.7 The latent heat, q release profiles determined for experiments in Nozzle T3

4.4. Onset conditions for heterogeneous nucleation of CO_2 on H_2O ice particle in Nozzles T1 and T3

The onset conditions for heterogeneous CO_2 nucleation measured in both Nozzles T1 and T3 are summarized in Table 2 and plotted in **Fig. 8**, together with the vapor pressures of CO_2 liquid and CO_2 solid, $p_{CO2(l)}$ and $p_{CO2(s)}$. Here the values $p_{CO2(l)}$ are estimated by extrapolating the empirical equation[24] for $217 \le T/K \le 276$. It is striking how the data corresponding to the same weight fraction of H_2O in a particular nozzle line up consistently.

In the legend of Fig. 8, the radii of gyration of the H_2O ice particles at the onset points, r_{G_on}, are also indicated. These were determined by SAXS as we explain below in Sections 4.5 and 4.6. In Nozzle T3, the onset conditions move towards lower saturation (lower partial pressure and/or higher temperature) as w_{H2O} (r_{G_on}) increases. Finally, the data at the highest w_{H2O} (largest r_{G_on}) in Nozzle T3 (open circles) seem to align closely with the data measured in Nozzle T1 on slightly larger particles (closed circles). The dependence of the onset conditions on r_{G_on} will be discussed further in Section 4.6.

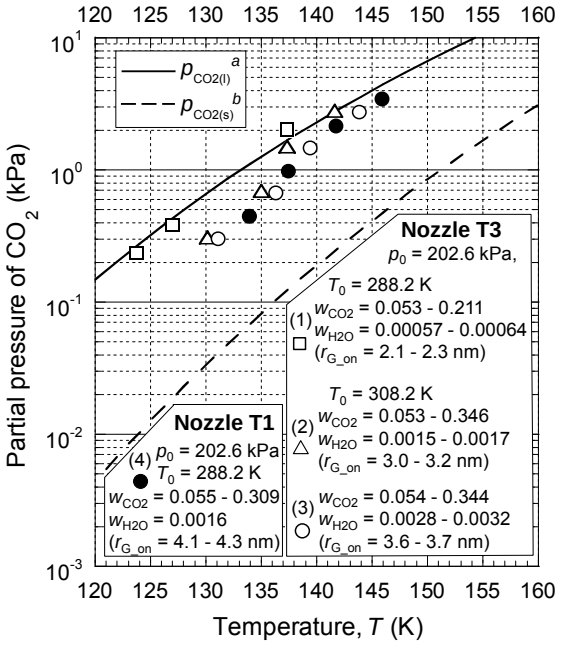

Fig.8 Onset conditions for heterogeneous nucleation of CO_2 on H_2O ice particles, p_{on_CO2} vs T_{on_CO2}.
The radii of gyration of H_2O ice particles at the onset points, r_{G_on} were determined by SAXS as described in Section 4.6.

[a] Equilibrium vapor pressure of CO_2 liquid. Equation in Ref.24 for $217 \le T/K \le 276$ is extrapolated towards supercooled temperature. (see Appendix 2)

[b] Equilibrium vapor pressure of CO_2 solid. (see Appendix 2)

4.5. Flow properties in Nozzle T1_mica and Nozzle T3_mica used in SAXS measurements

In order to make the SAXS measurements we used Nozzles T1_mica and T3_mica. These nozzles have mica windows mounted on the sidewalls as illustrated in Fig.15 of Appendix 1. **Fig. 9** shows the effective flow area ratios and temperature profiles in those nozzles, derived from the PTMs of pure N_2 flow. Near the throat the profiles agree reasonably well with those in Nozzle T1 and Nozzle T3, respectively, but deviations between the matched nozzles increase further downstream. The large deviations near z = ~8.5 cm, just downstream of the edge of the mica window, are attributed to the abrupt end of the window groove 8.38 cm downstream of the physical throat (see Fig. 15(a)). Since we cannot make SAXS measurements beyond the end of the window, these large deviations are irrelevant. As shown in Fig. 9(b), the temperature deviations between Nozzle T1_mica (T3_mica) and Nozzle T1 (T3) reflect the deviations in A/A^*.

Although a better match between the two sets of nozzles would be ideal, the differences do not impact our results because in the region where H_2O nucleation/ condensation occurs the expansion rates are actually quite close for matched nozzles. In particular, the average expansion rates are $d(A/A^*)_{dry}/dz$= 0.21 cm^{-1} in Nozzle T1 versus 0.22 cm^{-1} in Nozzle T1_mica between z = 0.6 cm and 1.3 cm, and $d(A/A^*)_{dry}/dz$ = 0.49 cm^{-1} in Nozzle T3 versus 0.50 cm^{-1} in Nozzle T3_mica between z = 0.5 cm and 1.5 cm. Similar expansion rates in this critical region of the nozzle should ensure that the size distributions of the H_2O ice particle produced during the SAXS experiments are almost the same as those produced during the PTMs.

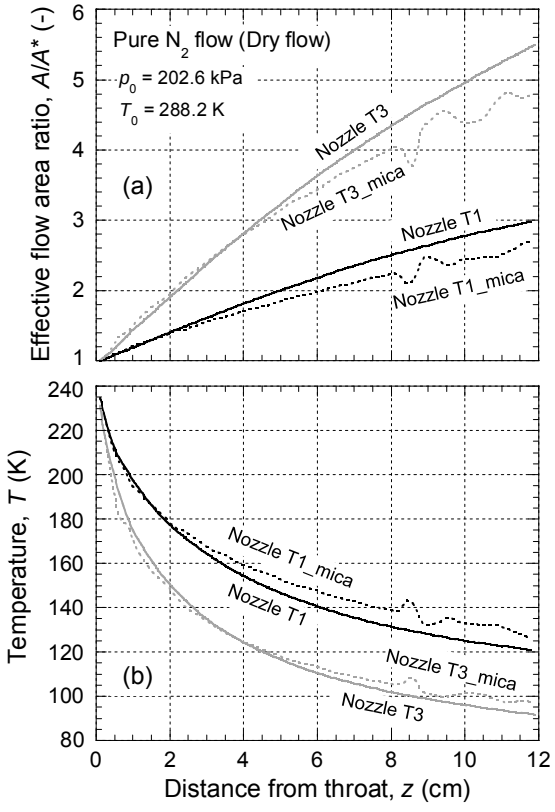

Fig.9 Flow properties in Nozzle T1_mica and Nozzle T3_mica. The deviation between the nozzles are discussed in the text.

4.6. Particle size from SAXS

Typical SAXS data are displayed on an absolute intensity scale in a Guinier plot in **Fig. 10**. The thick black lines are the fits to the data used to determine the radius of gyration, r_G, of the CO_2/H_2O particles. The values of r_G are shown in **Fig. 11** as a function of position in the nozzle, and the conditions corresponding to the experiments are summarized in Table 1. The rapid increase in particle size, 3 – 5 cm downstream of the throat, corresponds to the onset of CO_2 condensation. Upstream of the onset point, r_G is larger for higher values of w_{H2O} and/or when particles form in less rapidly expanding flows. These observations agree with our previous observations about H_2O and D_2O.[22,23,25] Furthermore, r_G does not show any systematic dependence on w_{CO2}, again emphasizing that CO_2 does not appear to play a role in the H_2O ice particle formation process.

In Nozzle T3_mica, the values of r_G at the onset point for heterogeneous nucleation of CO_2 on H_2O ice particle were determined by linearly extrapolating the values of r_G measured upstream of the onset point. In Nozzle T1_mica (T1,21 ~ T1,24), CO_2 only starts to condense when z = 6.7 - 8.5 cm, and thus, the r_G values at

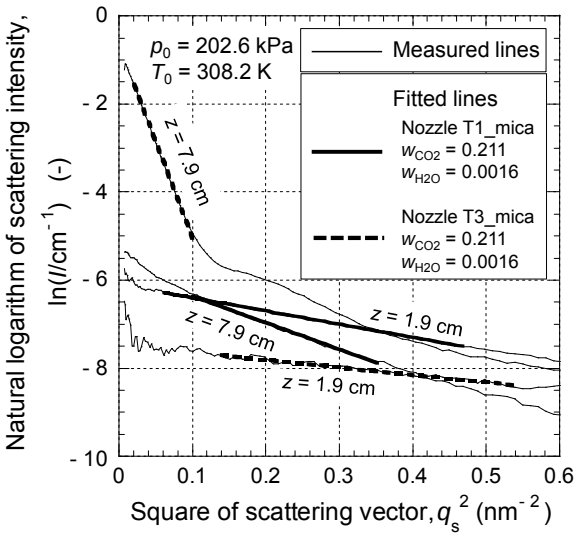

Fig.10 Typical Guinier plots of the SAXS data used to determine the radii of gyration of the particles.

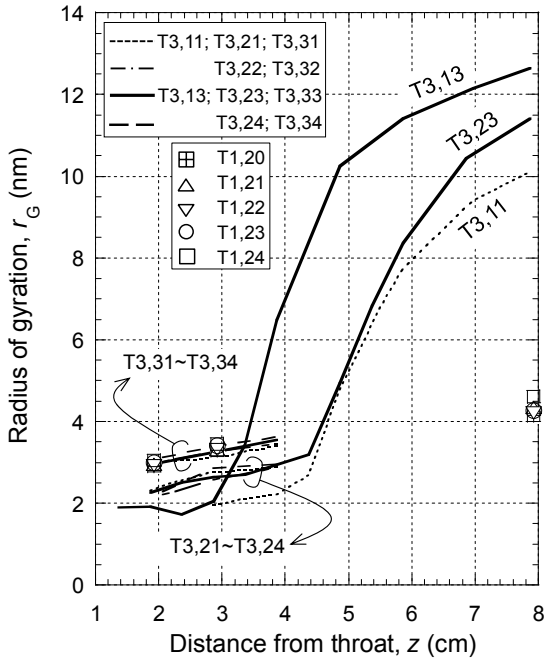

Fig.11 Radii of gyration determined from Guinier plots of SAXS spectra.
Flow conditions are indicated by the symbols in Table 1.

z = 1.9 and 2.9 cm in Fig. 11 are measured far upstream of the onset points. In these cases we extrapolated the r_G values at z = 2.9 cm to the corresponding onset points, by assuming that the slope (dr_G/dz) is equal to that determined for pure H_2O (T1,20) between z = 2.9 and 7.9 cm .

As illustrated in **Fig. 8**, the plots at almost the same r_G seem to lie along a line, and these lines move systematically toward lower saturation (lower partial pressure and/or higher temperature) as r_G increases, until the lines corresponding to (3) and (4) almost coincide. According to Fletcher's heterogeneous nucleation theory,[26] the rate of heterogeneous nucleation on a spherical particle increases with the radius of particle. The fact that the onset conditions (3) and (4) in Fig. 8 agree suggests that these values should be close to those for the heterogeneous nucleation of CO_2 on the flat H_2O ice surface at these saturations. Thus, we first directly compare our results, (3) and (4) in Fig. 8, to those of Glandorf et al.[10]

In Glandorf et al.'s FTIR experiments,[10] the onset of heterogeneous nucleation of CO_2 solid on a flat H_2O ice surface, i.e. the critical saturation for CO_2 solid $S_{CO2(s)}$, was $S_{CO2(s)}$ = 1.34 in the temperature range T = 130.2 - 140.0 K. Our experiments cover essentially the same temperature range but the lowest critical saturations with respect to the CO_2 solid, i.e. those for the results (3) and (4) in Fig. 8, are in the range $S_{CO2(s)}$ = 6.4 - 8.2, values that are much higher than those reported by Ref. 10.

One reason for the difference in $S_{CO2(s)}$ is that the timescales in the nozzle experiments are much shorter than those accessed by Ref. 10. In particular, in the FTIR studies, heterogeneous nucleation was observed within 10 s after the saturation of CO_2 reached the critical value (onset condition). In our study, the travel time from the point where $S_{CO2(s)}$ = 1.34 to the onset point is ~20 μs for results (3) and ~50 μs for results (4). A difference in time scales of 5 - 6 orders of magnitude should not, however, require such a large difference of the critical saturations. In Fig. 6 in Ref. 27, for example, the nucleation rate is estimated to increase by a factor of 10^7 when $S_{CO2(s)}$ is increased from 1.34 to 1.40 under conditions corresponding to the experiments in Ref. 10.

A possible explanation for the large difference in the onset conditions between the current study and the work of Ref. 10 is that heterogeneous nucleation of CO_2 onto the H_2O ice particles starts from the supercooled liquid phase rather than the solid phase on the ~50 μs timescale. This, in turn, suggests that freezing of the supercooled CO_2 liquid adsorbed on the surface of H_2O ice takes more than 50 μs under the conditions investigated here..

For heterogeneous nucleation of CO_2 to start from the supercooled liquid phase, the saturation of CO_2 with respect to the supercooled liquid, $S_{CO2(l)}$, must be equal to or greater than unity at the onset conditions determined here. Although the onset conditions corresponding to (3) and (4) in Fig. 8 are below the vapor-liquid equilibrium line (V-L line) extrapolated from the experimental equation for $217 \leq T/\mathrm{K} \leq 276$, there is no reason to assume that the extrapolated line accurately represents the V-L line in the supercooled state, and we expect the V-L line could lie on or below the plots of the onset conditions (3) and (4).

Our interpretation is consistent with the analysis of experimental results by Mensah,[28] where heterogeneous nucleation of Ar on H_2O ice particles (radius was expected to be larger than 20 nm) was observed in a cryogenic nucleation pulse chamber in the timescale of a few 10 ms. The onset pressures determined by Mensah at temperatures between 52K and 72 K (below the triple point 83.3 K), were about 2 - 5 times higher than the vapor pressure of Ar solid, and strongly suggested the heterogeneous nucleation of Ar on H_2O ice particles occurs from the supercooled liquid phase.

On the timescale of about 10 s, heterogeneous nucleation of CO_2 on an H_2O ice surface occurs in the solid phase as indicated in Ref. 10. At the beginning of the nucleation process, however, the CO_2 on the H_2O ice film may be liquid as found in this study, because Glandorf et al.'s experiments were done under conditions (temperature and saturation of CO_2) similar to our study. If this is true, then freezing of the supercooled CO_2 liquid deposited on the H_2O ice surface is required for heterogeneous nucleation to proceed at $S_{CO2(l)} < 1 \leq S_{CO2(s)}$. The time lag related to the freezing may be a reason why heterogeneous nucleation does not occur in the solid phase on the short timescale of our experiment. Further investigation is necessary to confirm this interpretation.

The dependence of the onset conditions on the radius for the smallest H_2O ice particles, (1) and (2) in Fig. 8, is also the subject for a future study.

5. Further discussion

5.1. Contact parameter between supercooled CO_2 liquid and H_2O ice

In order to predict the vapor-liquid equilibrium line of CO_2 from the onset conditions determined in this study, we first need to estimate the contact parameter of liquid CO_2 on H_2O ice. The contact parameters of solid CO_2 on H_2O ice, $m_{CO2(s)}$ and that of liquid CO_2 on H_2O ice, $m_{CO2(l)}$ are defined as,

$$m_{CO2(s)} = \frac{\sigma_{H2O} - \sigma_{H2O/CO2(s)}}{\sigma_{CO2(s)}}, \quad (3)$$

$$m_{CO2(l)} = \frac{\sigma_{H2O} - \sigma_{H2O/CO2(l)}}{\sigma_{CO2(l)}}, \quad (4)$$

where σ_{H2O}, $\sigma_{CO2(s)}$, and $\sigma_{CO2(l)}$ are the surface free energies of H_2O ice, CO_2 solid, and CO_2 liquid, respectively, and $\sigma_{H2O/CO2(s)}$ and $\sigma_{H2O/CO2(l)}$ denote the interfacial free energies between H_2O ice and CO_2 solid, and between H_2O ice and CO_2 liquid, respectively. The value of $m_{CO2(s)} = 0.952$ is that estimated by Glandorf et al.[10]

To estimate the value of $m_{CO2(l)}$ we substitute the values of the surface free energies,[27] $\sigma_{H2O} = 0.106$ J/m^2 and $\sigma_{CO2(s)} = 0.080$ J/m^2 into eqn (3) assuming $m_{CO2(s)} = 0.952$ to obtain $\sigma_{H2O/CO2(s)} = 0.030$ J/m^2. A Block equation,[29] using parameters obtained from experimental values of $\sigma_{CO2(l)}$ in the range $221.0 \leq T/\mathrm{K} \leq 293.2$, was extrapolated to the relevant temperature range, 130 to 140 K, and gave an average value of $\sigma_{CO2(l)} = 0.038$ J/m^2. Although the value of $\sigma_{H2O/CO2(l)}$ is not available in the literature, we can assume that $\sigma_{H2O/CO2(l)} < \sigma_{H2O/CO2(s)}$, based on the Duprés equation,[30] $\sigma_{H2O/CO2(l)} = \sigma_{H2O} + \sigma_{CO2(l)} - W_{H2O/CO2(l)}$ (for liquid CO_2), where $W_{H2O/CO2(l)}$ denotes the work of adhesion at the interface. As noted above, $\sigma_{CO2(l)} < \sigma_{CO2(s)}$ and $W_{H2O/CO2(l)}$ should be larger than $W_{H2O/CO2(s)}$ given that

liquid CO_2 can move more freely and find a more stable configuration on the interface than solid CO_2. Using these vales we estimate $m_{CO2(l)}$ as $m_{CO2(l)} > (0.106 - 0.030)/0.038 = 2 > 1$. Since the maximum possible value for the contact parameter is 1, this results suggests $m_{CO2(l)} = 1$ and the contact angle is zero, i.e. the CO_2 liquid fully wets the H_2O ice surface and the critical saturation of CO_2 on the flat H_2O ice surface is unity.

If these arguments are valid, the V-L line for supercooled CO_2 liquid should lie very close to curves (3) and (4) in Fig. 8. The fully wetting behavior of CO_2 molecules on H_2O ice surface at a temperature of 50 or 100 K observed in the molecular dynamics simulation[15] may be attributed to the supercooled CO_2 liquid in a period prior to the freezing, because the simulation time was 3.5 ns, which is much shorter than the 50 μs travel time in the supersonic flow between the onset point expected for CO_2 solid and the onset point for CO_2 liquid observed in this study.

5.2. Condensation of CO_2 on H_2O ice particle downstream of onset point

Even if the initial critical nucleus of CO_2 is liquid like, at these low temperatures CO_2 is unlikely to remain in this state for long. To investigate the progress of CO_2 condensation/deposition onto the H_2O ice particles we therefore extended the PTM analysis downstream to the nozzle exit. Since heat release is high and will affect the boundary layers in this region, we first determined $(A/A^*)_{wet}$ using the r_G values in Fig. 11 as follows.

The volume of condensed droplet per unit mass of gas mixture, V'_c can be approximately derived from r_G neglecting the effect of size distribution and assuming spherical shape as,

$$V'_c = N'_c(4\pi/3)r_G^3, \quad (5)$$

where N'_c denotes the number of droplets per unit mass of gas mixture and is assumed to be constant downstream of the onset point. On the other hand, V'_c can be determined from the mass fractions of the condensed CO_2 and H_2O derived from PTM, g_{CO2} and g_{H2O}, as,

$$V'_c = g_{CO2}/d_{CO2} + g_{H2O}/d_{H2O}, \quad (6)$$

where d_{CO2} and d_{H2O} are the densities of the condensed CO_2 and H_2O, respectively.

The effect of the deviation of $(A/A^*)_{wet}$ from $(A/A^*)_{dry}$ on the determination of mass fraction of condensate is negligible just downstream of the onset point as shown in Fig. 6 in Ref. 31. Hence we can determine N'_c so that V'_c in eqn (5) agrees with V'_c in eqn (6) just downstream of the onset point, where g_{CO2} and g_{H2O} are derived assuming $(A/A^*)_{wet} = (A/A^*)_{dry}$. Using this value of N'_c, we determined $(A/A^*)_{wet}$ so that V'_c in eqn (6) agree with V'_c in eqn (5) downstream of the onset point. In eqn (6), $d_{H2O} = 930$ kg/m^3 is an averaged value of the density of H_2O ice (Ih) in the temperature range $T = 130$ - 140 K, and $d_{CO2} = 1600$ kg/m^3 is the value used by Ref. 27 and corresponds to the density of CO_2 solid at $T = 168.2$ K,[32] and is very close to the density at the temperature in this analysis ($T = \sim 140$ K), 1630 kg/m^3. We used the density of CO_2 solid for analysis, though the heterogeneous nucleation of CO_2 was found to start in liquid phase as discussed above, because, the condensation/deposition of CO_2 after nucleation was found to proceed via the solid phase as explained below.

The values of $(A/A^*)_{wet}$ and V'_c determined using this analysis are shown in **Fig. 12**. As shown in Fig. 12(a), N'_c was determined to be 3.8 x 10^{18} kg^{-1} so that V'_c in eqn (5) agree with V'_c from PTM with $(A/A^*)_{dry}$ just downstream of the onset point. And then $(A/A^*)_{wet}$ was determined as indicated in Fig. 12(b) so that V'_c from PTM using $(A/A^*)_{wet}$ reproduces V'_c in eqn (5) well in the whole region downstream of the onset point as shown in Fig. 12(a).

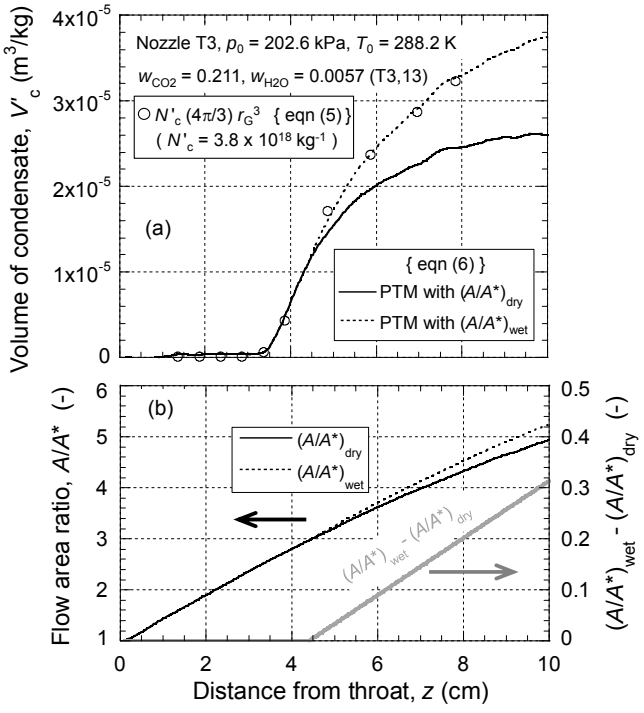

Fig.12 SAXS and PTM data were combined to determine the deviation of $(A/A^*)_{wet}$ from $(A/A^*)_{dry}$ downstream of the onset point for heterogeneous nucleation of CO_2 as described in the text.
(a) Volume of condensed droplet per unit mass of gas mixture, V'_c.
(b) Flow area ratio, A/A^*.

By using $(A/A^*)_{wet}$ determined above, the partial pressure of CO_2 and gas temperature in the condensing flow were derived and the partial pressure - temperature diagram, p_{v_CO2} - T line, are shown in **Fig. 13**. We restricted the p_{v_CO2} - T line to $z < 8$ cm, because the temperature is significantly underestimated for $z \geq$ ~8cm. The problem arises because the smaller expansion rate in Nozzle T3_mica relative to Nozzle T3 (Fig. 9(a)) leads to underestimated values of $r_{G,}$ and thus V'_c {eqn (5)} in Fig. 12(a) when $z >$ ~ 6 cm.

In Fig. 13 the onset points (3) and (4), that are expected to be very close to the V-L line of the supercooled CO_2 liquid, are also shown. The solid line is a tentative V-L line to guide the eye, where the slope of this line (that is the heat of vaporization) is constrained to be less than that of the solid. As shown in the figure, downstream of the onset point the p_{v_CO2} - T line crosses the V-L line and moves toward V-S line (vapor - solid equilibrium line), suggesting the supercooled CO_2 liquid adsorbed on the surface of H_2O ice freezes just after the nucleation/condensation start. The travel time between the onset point and the intersection of p_{v_CO2} - T line and V-L line is 28 μs, hence the freezing should occur within 28 μs at the most after the onset.

It is not yet known what triggers the freezing of the supercooled CO_2 liquid on H_2O ice particle. The decrease in temperature downstream of the onset point should not be the only trigger for freezing, because the nucleation is expected to start in liquid phase even at T = 124 K as shown in Fig. 8. Further investigation is necessary to elucidate the mechanism of the freezing of CO_2 adsorbed on the H_2O ice surface.

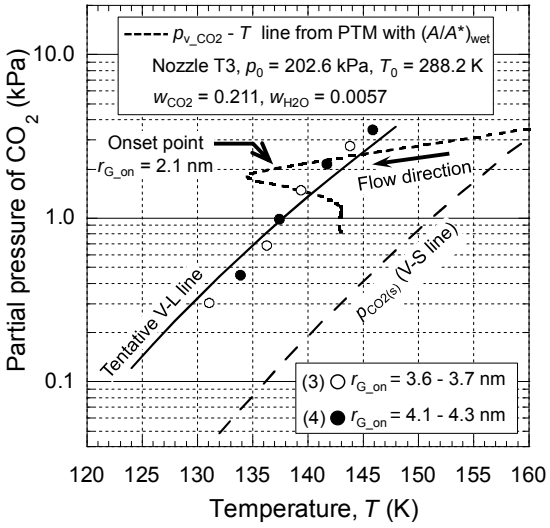

Fig.13 The expansion history is followed on a partial pressure - temperature diagram. The onset of CO_2 heterogeneous condensation is detected well before the lowest temperature reached in the expansion.

6. Conclusion

We have conducted the first systematic studies of heterogeneous nucleation in supersonic nozzles. Our findings contribute to elucidating the mechanism of heterogeneous nucleation, with particular reference to proposed innovative CO_2 capture technologies and cloud formation in the Martian atmosphere. We found that in the supersonic flow of gas mixture (CO_2 + H_2O + N_2) heterogeneous nucleation of CO_2 occurs on the H_2O ice particles produced by the homogeneous nucleation/condensation and freezing of H_2O. The data suggest that the heterogeneous nucleation of CO_2 may start from the supercooled liquid phase in the time scale of at least ~50 μs, and that the supercooled CO_2 liquid on the H_2O ice freezes just after the onset of the nucleation within at most ~30 μs and subsequent condensation proceeds in the solid phase.

Acknowledgments

We thank Anthony Castrogiovanni for his input and useful discussions during the course of the work. We thank Judith Wölk, S. Seifert and R. Winnans for their help in the SAXS experiments. The work was initially funded through the National Energy Technology Laboratory (NETL), DOE Carbon Capture Program, with Orbital ATK as a prime contractor (DE-FE0013122). Further support was provided by NSF grant CHE-1213959. This research used resources of the Advanced Photon Source, a U.S. Department of Energy (DOE) Office of Science User Facility operated for the DOE Office of Science by Argonne National Laboratory under Contract No. DE-AC02-06CH11357.

Appendix 1: Supersonic Laval nozzles used in this study

The supersonic nozzle is assembled from the symmetrically-arranged same-shaped two aluminum blocks in **Fig. 14(b)** and two flat side walls as shown by the cross section in **Fig. 14(a)**. The dimensions of the shaped block are shown in **Fig. 14(c)**. The nominal opening angle of the nozzle made of these blocks is 6.38°. For PTM, we assembled two nozzles with different throat height, h^*, from these blocks, namely, Nozzle T1 and Nozzle T3, where h^* = 0.500 cm for T1 and h^* = 0.211 cm for T3. The smaller h^* gives larger nominal expansion rate, $d(A/A^*)/dz'$, where A and A^* denote the cross section of the nozzle (nominal flow area) and that at the physical throat, respectively, and z' is the distance from the physical throat, where the nominal flow area has a minimum. When the Nozzle T1 is used, the third liquid N_2 Dewar was connected to the main flow, because the required N_2 flow was about 670 SLM.

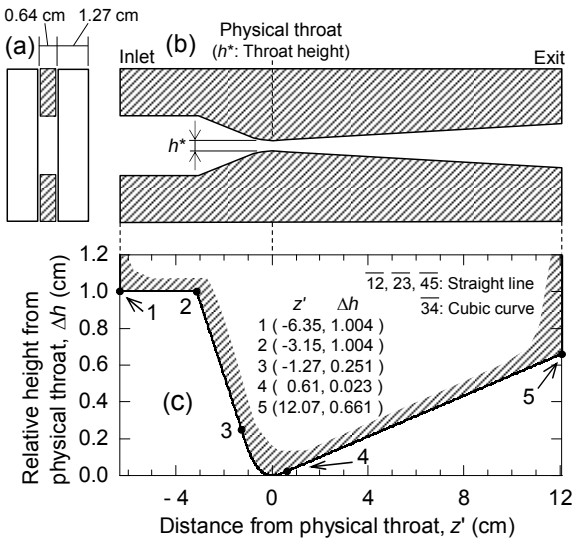

Fig.14 Supersonic Laval nozzle used in PTM.
(a) Cross section of assembled nozzle with flat side walls for PTM.
(b) Inner blocks determine the flow area of the nozzle.
(c) Dimension of the inner block.

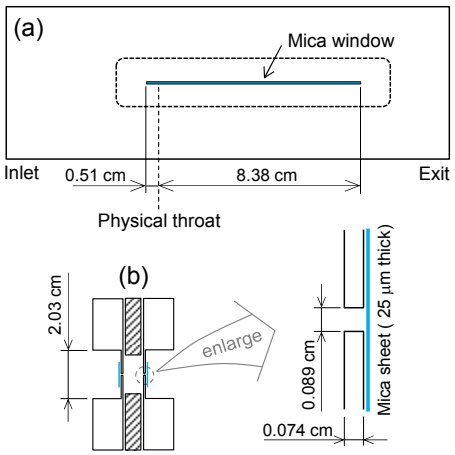

Fig.15 Supersonic Laval nozzle used in SAXS measurement.
(a) Side wall with a mica window
(b) Cross section of assembled nozzle with mica windows.

For SAXS experiments, we assembled Nozzle T1_mica and Nozzle T3_mica from the same shaped blocks as those for Nozzles T1 and T3, and from the sidewalls with mica window shown in **Fig. 15(a)**. As shown in the figure, mica window starts at 0.51 cm upstream from the physical throat and ends at 8.38

cm downstream. The cross section of the assembled nozzle is shown in **Fig. 15(b)**. As shown in the figure, the flow area in this nozzle includes the two of small rectangular (0.074 cm x 0.089 cm) in addition to the rectangular in the Nozzles T1 and T3 {see Fig. 14(a)}. Therefore, the throat height of Nozzle T1_mica (T3_mica) was set to 0.480 cm (0.191 cm) so that the nominal flow area of Nozzle T1_mica (T3_mica) is the same as that of Nozzle T1 (T3) for $-0.51 \leq z'/\mathrm{cm} \leq 8.38$.

Appendix 2: Thermodynamic properties of materials

Molar isobaric heat capacity of N_2 gas, $C_{p\_N2(v)} = 29.124$ J/mol K at $T = 298.15$ K was used. Ideal gas molar isobaric heat capacity of H_2O for $160 \leq T/\mathrm{K} \leq 340$ in Ref. 19 was extrapolated down to 110 K. The relative error caused by this extrapolation is less than 0.02 %.[33] The ideal gas molar isobaric heat capacity of CO_2 was obtained by fitting a quadratic function to the data for $100 \leq T/\mathrm{K} \leq 400$ in Ref. 34 as,

$$C^0_{p\_CO2(v)} = 25.92 + 2.930 \times 10^{-2}\, T + 2.38 \times 10^{-5}\, T^2 \quad \text{(J/mol K)}.$$

Vapor pressure of CO_2 solid is given in Ref. 35 as,

$$\log(p_{CO2(s)}/\mathrm{bar}) = 6.81228 - 1301.679/(T\text{-}3.494),$$

which well reproduces the data for $65 \leq T/\mathrm{K} \leq 195$ in Ref. 36. The heat of sublimation of CO_2 solid was obtained by applying the Clausius-Clapeyron equation to the $p_{CO2(s)}$ as,

$$\Delta h_{sub\_CO2} = 2.303R \times 1301.679\, T^2/(T\text{-}3.494)^2 \quad \text{(J/mol)}.$$

Vapor pressure of CO_2 liquid for $217 \leq T/\mathrm{K} \leq 276$ is given in Ref. 24 as,

$$\log(p_{CO2(l)}/\mathrm{atm}) = -1353.202/T - 8.142537 \log T + 6.259156 \times 10^{-3}\, T + 24.61930.$$

Vapor pressure and heat of vaporization of H_2O liquid for $123 \leq T/\mathrm{K} \leq 350$ in Ref. 19 were used extrapolating down to 110 K in this study. The accurate value of vapor pressure is not necessary for the analysis in this study as described in the explanation about eqn (1). The H_2O droplet is expected to be frozen at the onset point for the heterogeneous nucleation of CO_2 as described in the main text. However, at the onset temperature or less, the heat of vaporization of H_2O liquid is smaller than the heat of sublimation of H_2O solid (hexagonal or cubic ice) only by 3 %,[8] therefore, we can safely use the empirical equation

for the H_2O liquid without warring about where the H_2O droplet freeze in the supersonic nozzle.

Appendix 3: Correction of effective flow area ratio in condensing flow

As mentioned in the Section 3, $(A/A^*)_{wet}$ deviates from $(A/A^*)_{dry}$ downstream of the onset point, however, this deviation is small just downstream of the onset point and negligible for determination of the onset conditions for the typical homogeneous nucleations.[19] For determination of the onset conditions for heterogeneous nucleation of CO_2 on H_2O ice particle, however, the deviation of $(A/A^*)_{wet}$ from $(A/A^*)_{dry}$ may not be negligible, because $(A/A^*)_{wet}$ should be affected by the condensation of H_2O.

Figure 16 shows mass fraction ratio of H_2O in Nozzle T1, g_{H2O}/w_{H2O}, where g_{H2O} and w_{H2O} are the mass fractions of condensed H_2O and all H_2O, respectively. This value is expected to reach unity at z = 6 cm, where the condensation and freezing of H_2O should be completed as explained in Section 4.1. As shown in the figure, the values of g_{H2O}/w_{H2O} range 0.9 to 1.0 at z = 6 cm. These underestimations of g_{H2O}/w_{H2O} can be explained by the increase in $(A/A^*)_{wet}$ relative to $(A/A^*)_{dry}$, and should be accompanied by the underestimations of the temperature.[20] We adjusted the values of $(A/A^*)_{wet}$ so that g_{H2O}/w_{H2O} reach unity at z = 6 cm, and found the increases in the temperature due to these corrections are 0.3 K or less, which are negligibly small. Therefore, we approximated $(A/A^*)_{wet}$ as $(A/A^*)_{dry}$ for the analyses of the flows in Nozzle T1.

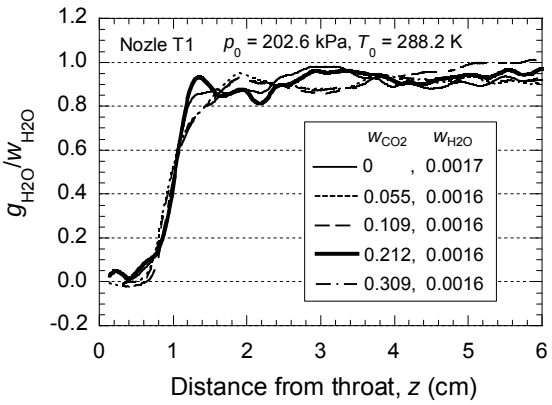

Fig.16 Mass fraction ratio of H_2O, g_{H2O}/w_{H2O}, where g_{H2O} and w_{H2O} are the mass fractions of condensed H_2O and all H_2O, respectively

In Nozzle T3, however, the effect of the deviation of $(A/A^*)_{wet}$ from $(A/A^*)_{dry}$ on the determination of temperature was estimeted to be about 1 K under the conditions in Figs. 7(b) and 7(c).Therefore, for the flows in Figs. 7(b) and 7(c), we determined the $(A/A^*)_{wet}$ so

that the mass fraction ratio, g_{H2O}/w_{H2O} reaches unity as shown in **Fig. 17** for a condensing flow as an example. As shown in Fig. 17(a), the g_{H2O}/w_{H2O} derived assuming $A/A^* = (A/A^*)_{dry}$ peaks at only about 0.75, therefore $(A/A^*)_{wet}$ was determined as shown in Fig. 17(b) so that g_{H2O}/w_{H2O} reaches unity as indicated in Fig. 17(a). We assumed a simple function for the deviation of $(A/A^*)_{wet}$ from $(A/A^*)_{dry}$ as shown in Fig. 17(b), that is, increases linearly and reaches a constant. This shape is consistent with our experimental results {Figs. 8(a) and 10(b) in Ref. 20}, where the change of the boundary-layer displacement thickness reaches a constant value downstream of the onset point of condensation. However, we neglectd the decrease of $(A/A^*)_{wet}$ (that is the increase of the displacement thickness) just downstream of the onset point shown in those figures in Ref. 20, because the change of $(A/A^*)_{wet}$ near the onset point of H_2O condensation (first onset point) should not affect the conditions at the onset point for the hetergeneous nucleation of CO_2, which is far downstream of the first onset point. The start point of the deviation of $(A/A^*)_{wet}$ was arbitrary set to the point where the slope of g_{H2O}/w_{H2O} has a maximum, and the endpoint of the increase was determined so that g_{H2O}/w_{H2O} peaks at unity except fluctuation by trial and error. The difference of the temperatures derived with $(A/A^*)_{wet}$ and with $(A/A^*)_{dry}$, $T_{(A/A^*)wet} - T_{(A/A^*)dry}$ is 1.2 K at most as shown in Fig. 17(c), and, under the conditions in this study, this difference was 1.4 K or less.

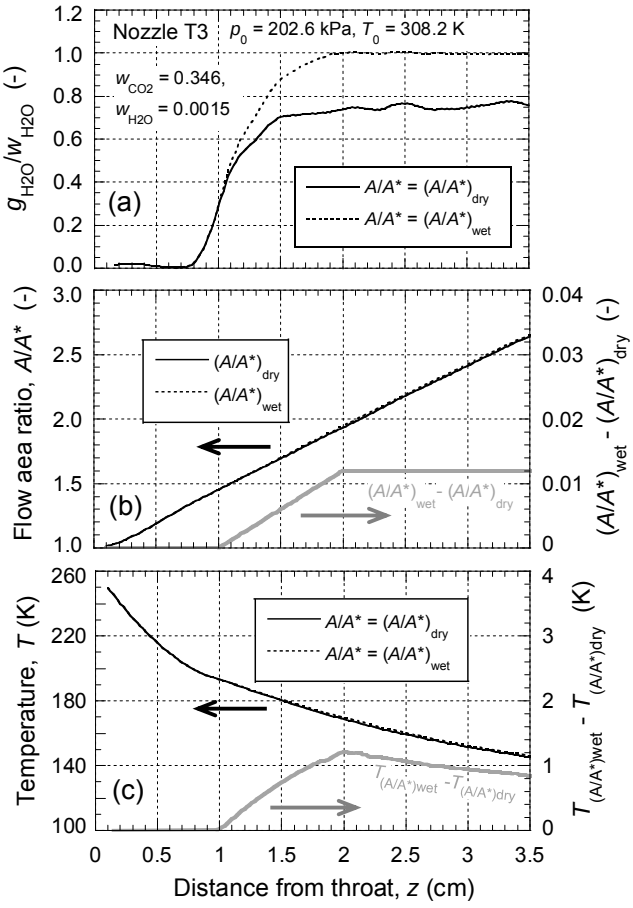

Fig.17 The correction to the flow area ratio in a condensing flow is required because heat addition compresses the boundary layers relative to the flow of carrier gas alone.
(a) Mass fraction ratio of H_2O, g_{H2O}/w_{H2O}.
(b) The effective flow area ratio, A/A^*.
(c) The gas temperatures derived with $(A/A^*)_{dry}$ or $(A/A^*)_{wet}$, $T_{(A/A^*)dry}$ and $T_{(A/A^*)wet}$ differ by less than 1.2 K.

References:

1 N. Sipöcz, A. Hernandez-Nogales, M. A. Gonzalez-Salazar, R. Shisler, and V. Lissianski, *Energy Procedia*, 2013, **37**, 1228-1238.

2 P. M. Sforza, A. Castrogiovanni, and R. Voland, *App. Therm. Eng.*, 2012, **49**, 154-160.

3 D. Berstad, R. Anantharaman, and P. Nekså, *Int. J. Refrigeration*, 2013, **36**, 1403-1416.

4 K. M. Duff, *NON-EQUILIBRIUM CONDENSATION OF CARBON DIOXIDE IN SUPERSONIC NOZZLES*, Doctor thesis, Massachusetts Institute of Technology, 1966.

5 A. Khan, C. H. Heath, U. M. Dieregsweiler, B. E. Wyslouzil, and R. Strey, *J. Chem. Phys.*, 2003, **119**, 3138-3147.

6 R. Span, W. Wagner, *J. Phys. Chem. Ref. Data*, 1996, **25**, 1509- 1596.

7 W. Wagner, A. Saul, and A. Pruss, *J. Phys. Chem. Ref. Data*, 1994, **23**, 515- 527.

8 D. M. Murphy and T. Koop, *Q. J. R. Meteorol. Soc.*, 2005, **131**, 1539-1565.

9 M. T. Ho, G. W. Allinson, and D. E. Wiley, *Int. J. Greenhouse Gas Control*, 2011, **5**, 49-60.

10 D. L. Glandorf, A. Colaprete, M. A. Tolbert, and O. B. Toon, *Icarus*, 2002, **160**, 66-72.

11 M. Isenor, R. Escribano, T. C. Preston, and R. Signorell, *Icarus*, 2013, **223**, 591-601.

12 J. A. Noble, E. Congiu, F. Dulieu, and H. J. Fraser, *Mon. Not. R. Astron. Soc.*, 2012, **421**, 768-779.

13 J. P. Devlin, C. A. Yinnon, and V. Buch, *Phys. Chem. Chem. Phys.*, 2009, **11**, 7819-7825.

14 M. Taraschewski, H. K. Cammenga, R. Tuckermann, and S. Bauerecker, *J. Phys. Chem.*, 2005, **109**, 3337-3343.

15 L. J. Karssemeijer, G. A. de Wijs, and H. M. Cuppen, *Phys. Chem. Chem. Phys.*, 2014, **16**, 15630-15639.

16 H. Laksmono, S. Tanimura, H. Allen, G. Wilemski, M. Zahniser, J. Shorter, D. Nelson, B. McManus, and B. E. Wyslouzil, *Phys. Chem. Chem. Phys.*, 2011, **13**, 5855-5871.

17 A. H. Shapiro, *The Dynamics and Thermodynamics of Compressible Fluid Flow*, Ronald, New York, 1953, vol. 1, ch. 4.

18 S. Tanimura, B. E. Wyslouzil, M. Zahniser, J. Shorter, D. Nelson, and J. B. McManus, *J. Chem. Phys.*, 2007, **127**, 034305.

19 S. Tanimura, U. M. Dieregsweiler, and B. E. Wyslouzil, *J. Chem. Phys.*, 2010, **133**, 174305.

20 S. Tanimura, Y. Zvinevich, B. E. Wyslouzil, M. Zahniser, J. Shorter, D. Nelson, and B. McManus, *J. Chem. Phys.*, 2005, **122**, 194304.

21 R. J. Roe, *Methods of X-Ray and Neutron Scattering in Polymer Science*, Oxford University, New York, 2000.

22 A. Manka, H. Pathak, Shinobu Tanimura, J. Wölk, R. Strey, and B. E. Wyslouzil, *Phys. Chem. Chem. Phys.*, 2012, **14**, 4505-4516.

23 Y. J. Kim, B. E. Wyslouzil, G. Wilemski, J. Wölk, and R. Strey, *J. Phys. Chem.*, 2004, **108**, 4365-4377.

24 A. Michels, T. Wassenaar, TH. Zwietering, and P. Smits, *Physica*, 1950, **16**, 501-504.

25 B. E. Wysouzil, G. Wilemski, R. Strey, S. Seifert, and R. E. Winans, *Phys. Chem. Chem. Phys.*, 2007, **9**, 5353-5358.

26 N. H. Fletcher, *J. Chem. Phys.*, 1958, **29**, 572-576; ibid, 1959, **31**, 1136-1137.

27 A. Määttänen, H. Vehkamäki, A. Lauri, S. Merikallio, J. Kauhanen, H. Savijärvi, and M. Kulmala, *J. Geophys. Res.*, 2005, **110**, E02002.

28 A. Mensah, *First Experimental Data on the Gas-Liquid Vapor Pressure Curve of Liquid Argon between 52K and 72K*, Diploma thesis, Universität zu Köln, 2005.

29 E. L. Quinn, *J. Am. Chem. Soc.*, 1927, **49**, 2704-2711.

30 R. Defay, I. Prigogine, A. Bellemans, and D. H. Everett, *Surface Tension and Adsorption*, Longmans, Green, Bristol, 1966.

31 P. Paci, Y. Zvinevich, S. Tanimura, B. E. Wyslouzil, M. Zahniser, J. Shorter, D. Nelson, and B. McManus, *J. Chem. Phys.*, 2004, **121**, 9964-9970.

32 D. M. Newitt, M. U. Pai, N. R. Kuloor, and J. A. W. Huggill, *Carbon Dioxide*, in *Thermodynamic Functions of Gases* Volume 1, edited by F. Din, Butterworths Scientific Publications, London, 1956.

33 A. S. Friedman and L. Haar, *J. Chem Phys.*, 1954, **22**, 2051 - 2058.

34 M. W. Chase, Jr, *J. Phys. Chem. Ref. Data*, 1998, Monograph 9, p643.

35 National Institute of Standards and technology, http://webbook.nist.gov/chemistry.

36 M. A. Aïnou, *Monatshefte für chemie*, 2005, **136**, 2017-2027.

Table 1. A summary of the experimental stagnation conditions including stagnation pressure, p_0, stagnation temperature, T_0, weight fraction of CO_2 (H_2O), w_{CO2} (w_{H2O}), and mole fraction of CO_2 {H_2O}, $(y_{CO2})_0$ {$(y_{H2O})_0$}. The values in the parentheses are the conditions in SAXS measurements.

Nozzle	p_0 (kPa)	T_0 (K)	w_{CO2} (-)	w_{H2O} (-)	$(y_{CO2})_0$ (-)	$(y_{H2O})_0$ (-)	Symbol
T1 (T1_mica)	202.6	288.2	0 (0)	0.0017 (0.0017)	0 (0)	0.0026 (0.0027)	T1,20
			0.055 (0.056)	0.0016 (0.0017)	0.036 (0.037)	0.0026 (0.0027)	T1,21
			0.109 (0.109)	0.0016 (0.0016)	0.072 (0.072)	0.0026 (0.0027)	T1,22
			0.212 (0.210)	0.0016 (0.0016)	0.146 (0.144)	0.0027 (0.0026)	T1,23
			0.309 (0.281)	0.0016 (0.0015)	0.222 (0.200)	0.0027 (0.0027)	T1,24
			0.210	0	0.145	0	T1,03
T3 (T3_mica)	202.6	288.2	0.037	0.00060	0.024	0.0010	T3,10
			0.053 (0.054)	0.00064 (0.00062)	0.035 (0.035)	0.0010 (0.0010)	T3,11
			0.211 (0.210)	0.00057 (0.00061)	0.146 (0.145)	0.0010 (0.0010)	T3,13
		308.2	0.054 (0.054)	0.0017 (0.0016)	0.035 (0.035)	0.0026 (0.0026)	T3,21
			0.106 (0.106)	0.0017 (0.0016)	0.070 (0.070)	0.0027 (0.0027)	T3,22
			0.211 (0.210)	0.0016 (0.0016)	0.145 (0.145)	0.0026 (0.0027)	T3,23
			0.346 (0.343)	0.0015 (0.0015)	0.252 (0.250)	0.0026 (0.0026)	T3,24
			0.054 (0.054)	0.0032 (0.0032)	0.035 (0.035)	0.0051 (0.0050)	T3,31
			0.104 (0.106)	0.0031 (0.0031)	0.069 (0.070)	0.0049 (0.0050)	T3,32
			0.211 (0.210)	0.0031 (0.0030)	0.145 (0.144)	0.0051 (0.0050)	T3,33
			0.344 (0.343)	0.0028 (0.0028)	0.250 (0.250)	0.0050 (0.0050)	T3,34

Table 2. Onset conditions for heterogeneous nucleation of CO_2 on H_2O ice particle in supersonic flow, partial pressure of CO_2, p_{on_CO2}, temperature, T_{on_CO2}, and radius of gyration of H_2O ice particle, r_{G_on}.

Nozzle	Symbol	p_{on_CO2} (kPa)	T_{on_CO2} (K)	r_{G_on}.(nm)
Nozzle T1	T1,21	0.45	133.9	4.3
	T1,22	0.98	137.4	4.2
	T1,23	2.2	141.7	4.2
	T1,24	3.5	145.9	4.1
Nozzle T3	T3,10	0.24	123.7	2.3[a]
	T3,11	0.38	126.9	2.2
	T3,13	2.0	137.4	2.1
	T3,21	0.31	130.2	3.2
	T3,22	0.70	135.0	3.1
	T3,23	1.5	137.4	3.0
	T3,24	2.8	141.7	3.1
	T3,31	0.30	131.0	3.6
	T3,32	0.68	136.3	3.6
	T3,33	1.5	139.4	3.7
	T3,34	2.8	143.8	3.7

[a] r_{G_on} for T3,10 was determined by linearly extrapolating the two r_{G_on} for T3,11 and T3,13 to the onset point for T3,10.

Heterogeneous nucleation of CO_2 on H_2O ice particles in supersonic nozzle